A thermal multi-phase flow model for directed energy deposition processes via a moving signed distance function

Ze Zhao, Qiming Zhu, Jinhui Yan[*]

Department of Civil and Environmental Engineering, University of Illinois at Urbana-Champaign, United States of America

Abstract

Thermal multi-phase flow analysis has been proven to be an indispensable tool in metal additive manufacturing (AM) modeling, yet accurate and efficient simulations of metal AM processes remains challenging. This paper presents a flexible and effective thermal multi-phase flow model for directed energy deposition (DED) processes. Departing from the data-fitted or presumed deposit shapes in the literature, we first derive a deposit geometry model based on an energy minimization problem with a mass conservation constraint. Then, an interface-capturing approach based on a signed distance function that moves with the laser is constructed to represent the air–metal interface evolution. The approach can be applied to any type of mesh without requiring the activation process of solid elements in a mesh. The coupled multi-phase Navier–Stokes and energy conservation equations are solved by a variational multi-scale formulation (VMS). A density-scaled continuous surface force (CSF) model is employed to incorporate the Marangoni effect, no penetration boundary condition, and the heat source on the air–metal interface. We utilize the proposed method to simulate two representative metal manufacturing problems. The simulated results are carefully compared with available experimental measurements and computational results from others. The results demonstrate the accuracy and modeling capabilities of the proposed method for metal AM problems.
© 2020 Elsevier B.V. All rights reserved.

Keywords: Directed energy deposition; Additive manufacturing; Thermal multi-phase flow; Variational multi-scale formulation

1. Introduction

Metal additive manufacturing (AM), such as laser powder bed fusion (LPBF) and directed energy deposition (DED), has the potential to revolutionize mechanical, aerospace, and biomedical industries owing to the superior capability to print metals with complex geometries directly from digital models without the constraints of traditional manufacturing technologies [1]. Developing predictive models to link the process–structure–property is one of the fundamental research areas in metal AM. However, metal AM, due to the intrinsic multi-scale and multi-physics nature, is challenging to model. For the past decade, many researchers have proposed various methods to model metal AM at different scales.

Among the essential models is the process modeling technique, which acts as a spearhead to elucidate the driving physics of manufacturing processes and their dependence on process parameters. The state-of-the-art metal AM process modeling techniques employ thermal fluid models by solving Navier–Stokes equations coupled with heat transfer at the powder scale to capture the evolution of temperature, melt pool dynamics, phase transition,

---

* Corresponding author.
  E-mail address: yjh@illinois.edu (J. Yan).

and interface topological changes. Lawrence Livermore National Lab developed a thermal-fluid solver using the Arbitrary-Lagrangian Eulerian technique [2–5]. Lin et al. [6,7] developed a control-volume finite element approach to simulate a single particle deposition during DED processes. Yan et al. utilized the volume-of-fluid (VoF) based thermal-fluid solver to model multi-layer and multi-track LPBF processes [8–12]. Panwisawas et al. also employed the VoF method by using OpenFOAM to analyze the inter-layer and inter-track void formation [13]. Li et al. developed a thermal-fluid model by combining the level set method and Lagrangian particle tracking to investigate powder–gas interaction in LPBF processes [14].

Despite the fine resolved details, the computational cost of these powder-scale approaches is prohibitively high due to the small size and the large number of powders during metal AM processes. An alternative approach to reduce the computational cost is to treat powders as continuous domain and not discrete ones. For directed energy deposition simulations, this type of approach's success largely depends on deposit geometry models. A recent paper by Wang et al. [15] performed a thorough analysis of deposit geometry using power-scale multi-physics modeling and gaussian process regression analysis. However, in the context of continuous domain based analysis, previous models typically utilize experimental data-fitted shapes or presumed 2D or 3D geometry shapes, such as parabolic, sinusoidal or elliptical surfaces [16–20]. These approaches are easy to use but lack a solid physical foundation. Besides, the materials deposit process of these approaches is achieved by activating the mesh elements as solids as the laser scans, which restricts the types of elements allowed in the simulations [21].

Departing from these approaches, we put forth an effective gas–liquid–solid thermal fluid model without introducing any additional equation to simulate DED processes. We first derive a theoretical model for the deposit geometry based on an energy minimization problem subject to a mass conservation constraint. Then, an interface-capturing approach based on a signed distance function that moves with the laser is utilized to represent the air–metal interface. The Marangoni effect, no penetration boundary condition, and the laser heat are handled by the density-scaled continuous surface force (CSF) model [22] that is also used in our previous multi-phase flow work in [7,23–25]. We solve the thermal fluid model by employing the residual-based variational multiscale formulation (VMS). VMS, attributed to its geometry flexibility and variational consistency, has been applied to many challenging computational fluid dynamics (CFD), fluid–structure interaction (FSI), and multi-physics problems [26–31], rendering it very attractive to thermal multi-phase flow problems in metal AM processes.

This paper is structured as follows. Section 2 describes the thermal multi-phase flow formulation, including governing equations, deposit geometry model, interface-capturing approach, and VMS formulation. Section 3 presents the applications to two metal manufacturing problems. The simulated results are carefully compared with experimental data or computational results from others to demonstrate the proposed approach's accuracy and predictive capability. We summarize the contributions and limitations of the proposed method in Section 4.

2. Formulation

The proposed multi-phase flow formulation considers gas, liquid, and solid phases during DED processes. The air and metal phases are distinguished by an interface-capturing approach, while the liquid and solid metal phases are distinguished by a liquid fraction that is a function of temperature. The formulation builds upon the tacit assumption that the solid phase is a highly viscous fluid with the same constant density as the liquid metal. The latent heat of fusion is considered, while the loss of metal material due to vaporization and the effects on heat loss, composition change, and fluid motion are negligible for the problems considered here.
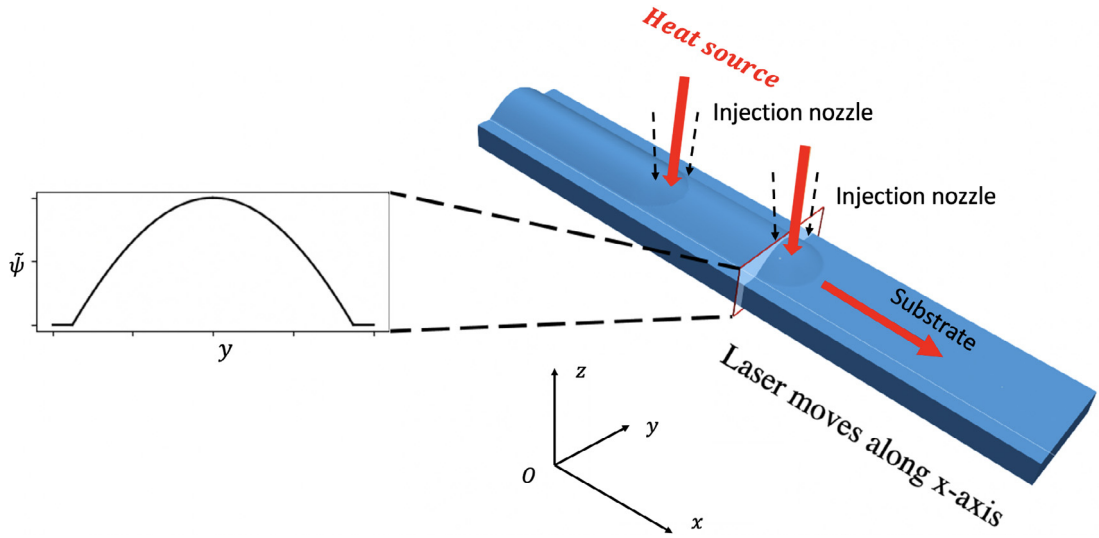
2.1. Governing equations

The gas, liquid, and solid phases in DED processes are modeled by a unified fluid mechanics approach, in which the material properties are interpolated by the respective properties of individual phases. The velocity $\mathbf{u}$, pressure p, and temperature T during DED processes satisfy the following incompressible Navier–Stokes equations and energy conservation equation.

$$r_M(\mathbf{u}, p) := \frac{\partial \rho \mathbf{u}}{\partial t} + \nabla \cdot (\rho \mathbf{u} \otimes \mathbf{u}) + \nabla p - \nabla \cdot (2\mu \nabla^s \mathbf{u}) - \rho \mathbf{g} - \mathbf{f}_s - \mathbf{f}_p = \mathbf{0} \qquad in\ \mathbf{\Omega_t} \qquad (1)$$

$$r_C(\mathbf{u}) := \nabla \cdot \mathbf{u} = 0 \qquad in\ \mathbf{\Omega_t} \qquad (2)$$

$$r_T(\mathbf{u}, T) := \frac{\partial (\rho h)}{\partial t} + \nabla \cdot (\rho \mathbf{u} h) - \nabla \cdot (\kappa \nabla T) - Q_T = 0 \qquad in\ \mathbf{\Omega_t} \qquad (3)$$

Fig. 1. Diagram of a single-track DED process. As the laser moves, the surrounding nozzles simultaneously inject metallic powders into the laser beam and deposit them onto the substrate.

where $\boldsymbol{\Omega_t}$ is the problem domain, ρ and μ are the material density and dynamic viscosity, $\mathbf{g}$ is the gravitational acceleration vector, ∇^s is the symmetric part of gradient operator. In Eq. (3), $h = \int_{T_0}^{T} c_p d\tau + Lf_L$ is the enthalpy, where c_p is the heat capacity, κ is the heat conductivity, L is the latent heat of fusion, and f_L is the liquid fraction that takes a linear profile in the mushy zone, namely,

$$f_L(T) = \begin{cases} 0, & T \leq T_s \\ \frac{T-T_s}{T_l-T_s}, & T_s < T < T_l \\ 1, & T_l \leq T \end{cases} \tag{4}$$

where T_s and T_l are the solidus and liquidus temperature, respectively.

In Eqs. (1)–(3), $\mathbf{f}_s$, $\mathbf{f}_p$, and Q_T represent the Marangoni force, non-penetration boundary condition, and heat laser on the gas–metal interface, respectively. We will present the respective models based on an interface-captured approach later in the paper.

2.2. Deposit geometry

Deposit geometry is an important factor for DED simulations. Previous models either rely on experimental observations or presumed 2D/3D geometry shapes, such as parabolic, sinusoidal or elliptical surfaces [16–20]. These models are simple to implement but lack a sound physical foundation. Departing from these models, we propose a new theoretical approach to derive the deposit geometry based on an energy minimization problem with mass conservation constraint. Fig. 1 shows the schematic diagram of a typical single-track DED process. The proposed approach makes two assumptions: (1) The cross-section of the deposit remains unchanged behind the laser. (2) The material distribution is radially symmetric under the laser beam. To derive the deposit shape, we first define the following energy function in the deposit volume.

$$E = \int_{\boldsymbol{\Gamma}_t} \sigma d\Gamma + \int_{\boldsymbol{\Omega}_t^{ded}} \rho_m gz d\Omega \tag{5}$$

where $\boldsymbol{\Omega}_t^{ded}$ is the volume occupied by the material deposit, $\boldsymbol{\Gamma}_t$ is the surface of $\boldsymbol{\Omega}_t^{ded}$ exposed to the air. In Eq. (5), the first term represents the surface energy, where σ is the surface tension coefficient. The second term is the gravitational potential energy, where ρ_m is the metal density, g is the gravitational acceleration magnitude, z is the height with respect to the substrate. The deposit geometry $\boldsymbol{\Gamma}_t$ can be described as a height function $\psi(x, y)$ with

respect to the substrate (x-y plane), namely,

$$\boldsymbol{\Gamma}_t = \{\mathbf{x} = (x, y, z)^T | z = \psi(x, y), \mathbf{x} \in \mathbb{R}^3\} \tag{6}$$

Then, the total energy function in Eq. (5) can be expressed as

$$E(\psi) = \int_{\boldsymbol{\Gamma}_t^p} (\sigma \sqrt{1 + \psi_{,x}^2 + \psi_{,y}^2} + \frac{1}{2} \rho_m g \psi^2) dx dy \tag{7}$$

where $\boldsymbol{\Gamma}_t^p$ is the projection of $\boldsymbol{\Gamma}_t$ on the substrate. $\psi(x, y)$ can be obtained by minimizing the energy function $E(\psi)$ subject to appropriate constraints. Considering the caught mass from the nozzle must equal the mass in the deposit volume, the following constraint needs to be satisfied, $\rho_m V_s A = \eta_c \dot{m}$, where A is the area of the cross-section behind heat laser, η_c is the fractional mass catchment of material into the melt pool, $\dot{m}$ is the mass flow rate from the nozzle, V_s is the scanning speed of the laser. Considering the facts that the deposit cross-section behind the laser remains unchanged and the deposit length is much longer than its width, it is reasonable to assume $\psi_{,x} = 0$ in Eq. (7), which reduces the 3D minimization problem to the following 2D minimization problem

$$\tilde{\psi} = \operatorname*{argmin}_{\tilde{\psi}} \qquad \tilde{E}(\tilde{\psi}) = \int_{-\frac{L}{2}}^{\frac{L}{2}} (\sigma \sqrt{1 + \tilde{\psi}_{,y}^2} + \frac{1}{2} \rho_m g \tilde{\psi}^2) dy \tag{8}$$

$$\text{subject to} \qquad \rho_m V_s \int_{-\frac{L}{2}}^{\frac{L}{2}} \tilde{\psi} dy = \eta_c \dot{m}$$

where $\tilde{\psi} = \tilde{\psi}(y)$ is the height function of the deposit cross-section behind the laser (see Fig. 1), L is the deposit width, which is a fraction f_m of the laser beam radius r_b. f_m varies from 0.75 and 1, depending on the manufacturing parameters [20].

The minimization problem in Eq. (8) can be solved by using a Lagrangian multiplier approach, in which the following Lagrangian functional is defined

$$F(\tilde{\psi}) = \tilde{E}(\tilde{\psi}) + \lambda \left(\rho_m V_s \int_{-\frac{L}{2}}^{\frac{L}{2}} \tilde{\psi} dy - \eta_c \dot{m} \right) \tag{9}$$

where λ is an unknown Lagrangian multiplier. The stationary point is obtained by setting $\frac{\delta F}{\delta \tilde{\psi}} = 0$ and $\frac{\delta F}{\delta \lambda} = 0$, which leads to the following two Euler–Lagrange equations with boundary conditions.

$$\tilde{\psi}_{,yy} = \frac{\frac{\rho g \tilde{\psi} + \lambda}{\sigma} \sqrt{1 + \tilde{\psi}_{,y}^2} + \tilde{\psi}_{,y}^2}{1 + \tilde{\psi}_{,y}^2} \tag{10}$$

$$\int_{-\frac{L}{2}}^{\frac{L}{2}} \tilde{\psi} dy = \frac{\eta_c \dot{m}}{\rho_m V_s} \tag{11}$$

$$\tilde{\psi}(\pm \frac{L}{2}) = 0 \tag{12}$$

This is a highly nonlinear ordinary differential equation (ODE) and has to be solved numerically. The good news is that we only need to solve it once. Once $\tilde{\psi}$ is given, the deposit geometry $\boldsymbol{\Gamma}_t$ is constructed as follows. The deposit behind the laser is obtained by extruding $\tilde{\psi}$ along x direction, and the deposit front is obtained by rotating $\tilde{\psi}$ around the laser. With $\boldsymbol{\Gamma}_t$, a signed distance function that moves with the laser at the same speed is constructed to represent the air–metal interface. The approach and the associated methods of enforcement boundary conditions on the air–metal interface will be given next.

2.3. Interfacial method

We make use of an interface-capturing method to handle the gas–metal interface. To this end, a signed distance function $\phi(t, \boldsymbol{x})$ is defined in $\boldsymbol{\Omega}_t$. $\phi = 0$ on the air–metal interface and takes a signed distance with respect to the

deposit geometry Γ_t in air and metal phases, given as follows

$$\phi(t, \boldsymbol{x}) = \begin{cases} dist(\boldsymbol{x}, \Gamma_t) & \text{if } \boldsymbol{x} \in \Omega_m \\ 0 & \text{if } \boldsymbol{x} \in \Gamma_t \\ -dist(\boldsymbol{x}, \Gamma_t) & \text{if } \boldsymbol{x} \in \Omega_a \end{cases} \tag{13}$$

$\phi(t, \boldsymbol{x})$ can be obtained by solving the following Eikonal equation

$$\|\nabla\phi\| = 1 \text{ in } \boldsymbol{\Omega_t} \tag{14}$$

$$\phi = 0 \text{ on } \Gamma_t \tag{15}$$

With the signed distance function ϕ, any material χ needed in the thermal fluid equations can be evaluated by the following interpolation.

$$\chi(\phi, t) = \chi_a \left[1 - H_\epsilon(\phi)\right] + \left[\chi_l f_L + \chi_s (1 - f_L)\right] H_\epsilon(\phi) \tag{16}$$

where χ_a, χ_l, and χ_s are the corresponding material property in air, liquid, and solid phases. H_ϵ is a regularized Heaviside function, given as

$$H_\epsilon(\phi) = \begin{cases} 0 & \text{if } \phi \leq -\epsilon \\ \frac{1}{2}(1 + \frac{\phi}{\epsilon} + \frac{1}{\pi} sin(\frac{\pi\phi}{\epsilon})) & \text{if } |\phi| < \epsilon \\ 1 & \text{if } \phi \geq \epsilon \end{cases} \tag{17}$$

where ϵ is a small, positive constant and scales with local element size, which defines the air–metal interface thickness.

Continuous surface force (CSF) model [22] is used to incorporate the boundary conditions of the Marangoni effect and no penetration boundary condition on the air–metal interface in the Navier–Stokes equations, and heat flux in the energy conservation equation. The basic concept of the CSF model is converting traction/flux type boundary conditions into volumetric forcing terms via a regularized Dirac-δ function δ_ϵ that is only non-zero around the gas–metal interface. In present formulation, $\mathbf{f}_s$, $\mathbf{f}_p$, and Q_T are defined as

$$\mathbf{f}_s = \frac{\partial\sigma}{\partial T}\left[\nabla T - (\nabla T \cdot \mathbf{n})\mathbf{n}\right]\delta_\epsilon \tag{18}$$

$$\mathbf{f}_p = -\lambda_p(\mathbf{u} \cdot \mathbf{n})\mathbf{n}\delta_\epsilon \tag{19}$$

$$Q_T = \frac{d\eta_p Q}{\pi r_b^2} exp(-d\frac{|\mathbf{x} - \mathbf{x_c}|^2}{r_b^2})(\mathbf{n} \cdot \mathbf{e}_3)\delta_\epsilon \tag{20}$$

where $\mathbf{n}$ is the unit normal vector of gas–metal interface, $\mathbf{e}_3 = (0, 0, 1)^T$, $\frac{\partial\sigma}{\partial T}$ is the Marangoni coefficient, λ_p is a penalty coefficient for no penetration boundary condition, Q is the laser power, d is the laser distribution factor, η_p is the absorptivity, r_b is the laser radius, $\mathbf{x}_c$ is the laser center that moves with scanning speed V_s. Normally, δ_ϵ can calculated as $\delta_\epsilon = \frac{\partial H_\epsilon}{\partial\phi}$. Following our previous work in [7,23], the density-scaled Dirac-δ function is utilized, namely,

$$\delta_\epsilon(\phi) = \frac{2\rho(\phi)}{\rho_a + \rho_s}\frac{\partial H_\epsilon}{\partial\phi} \tag{21}$$

2.4. Variational multi-scale formulation

A residual-based variational multi-scale approach (VMS) [32,33] is employed to solve the above thermal multi-phase flow model for DED processes. For completeness, the semi-discrete formulation is briefly presented as follows. Let $\mathcal{V}^h$ denote the trial function space for unknown velocity $\mathbf{u}^h$, pressure p^h, and temperature T^h, respectively. Let $\mathcal{W}^h$ denote the space of test functions $\{\mathbf{w}^h, q^h, \eta^h\}$ for the momentum, continuity, and energy conservation equations, respectively. The VMS formulation of the thermal multi-phase flow model is stated as: $\forall\{\mathbf{w}^h, q^h, \eta^h\} \in \mathcal{W}^h$, find $\{\mathbf{u}^h, p^h, \phi^h\} \in \mathcal{V}^h$, such that

$$\int_{\Omega_t} \mathbf{w}^h \cdot \left[\frac{\partial \rho \mathbf{u^h}}{\partial t} + \nabla \cdot (\rho \mathbf{u}^h \otimes \mathbf{u}^h) - \rho \mathbf{g} - \mathbf{f}_s - \mathbf{f}_p \right] d\Omega - \int_{\Omega_t} p^h \nabla \cdot \mathbf{w}^h d\Omega$$

$$- \int_{\Gamma_F} \mathbf{w}^h \cdot \mathbf{h} d\Gamma + \int_{\Omega_t} \nabla \mathbf{w}^h : 2\mu \nabla^s \mathbf{u}^h d\Omega + \int_{\Omega_t} q^h \nabla \cdot \mathbf{u}^h d\Omega$$

$$+ \int_{\Omega_t} \eta^h \left[\frac{\partial (\rho h^h)}{\partial t} + \nabla \cdot (\rho \mathbf{u}^h h^h) \right] d\Omega + \int_{\Omega_t} \nabla \eta^h \cdot \kappa \nabla T^h d\Omega - \int_{\Gamma_T} \eta^h q d\Gamma - \int_{\Omega_t} \eta^h Q_T d\Omega$$

$$+ \Sigma_{e=1}^{n_{el}} \int_{\Omega_t^e} \tau_M (\mathbf{u}^h \cdot \nabla \mathbf{w}^h + \frac{\nabla q^h}{\rho}) \cdot \mathbf{r}_M (\mathbf{u}^h, p^h) d\Omega$$

$$+ \Sigma_{e=1}^{n_{el}} \int_{\Omega_t^e} \rho \tau_C \nabla \cdot \mathbf{w}^h r_C(\mathbf{u}^h) d\Omega - \Sigma_{e=1}^{n_{el}} \int_{\Omega_t^e} \tau_M \mathbf{w}^h \cdot [\mathbf{r}_M(\mathbf{u}^h, p^h) \cdot \nabla \mathbf{u}^h] d\Omega$$

$$- \Sigma_{e=1}^{n_{el}} \int_{\Omega_t^e} \frac{\nabla \mathbf{w}^h}{\rho} : \tau_M \mathbf{r}_M (\mathbf{u}^h, p^h) \otimes \tau_M \mathbf{r}_M (\mathbf{u}^h, p^h) d\Omega$$

$$+ \Sigma_{e=1}^{n_{el}} \int_{\Omega_t^e} \tau_T \mathbf{u}^h \cdot \nabla \eta^h r_T(\mathbf{u}^h, T^h) d\Omega = 0 \qquad (22)$$

where the superscript h represents the scales of quantities resolved on the mesh used. The computational domain is decomposed into n_{el} elements, namely, $\Omega_t = \bigcup_e \Omega_\mathbf{t}^\mathbf{e}$. $\mathbf{r}_M$, r_C, and r_T represent the residuals of strong form governing equations in Eqs. (1)–(3). $\int_{\Gamma_F} \mathbf{w}^h \cdot \mathbf{h} d\Gamma$ and $\int_{\Gamma_T} \eta^h q d\Gamma$ are used for incorporating the traction $\mathbf{h}$ and heat flux q that are not applied on the gas–metal interface. Eq. (22) features an extension of the residual-based VMS of single-phase turbulent flows, first introduced in [33], to thermal multi-phase flows. The first two lines and the third line in Eq. (22) are the Galerkin formulation of the Navier–Stokes equations and energy conservation equation, respectively. The rest terms in Eq. (22) can be interpreted as a stabilized method or large eddy simulation (LES) turbulence model [27,33–42] for multi-phase fluid dynamics. τ_M, τ_T, and τ_C are the streamline upwind Petrov–Galerkin (SUPG) [34] and pressure-stabilizing Petrov–Galerkin (PSPG) [35] stabilization parameters, which are defined as below

$$\tau_M = \left[\frac{4}{\Delta t^2} + \mathbf{u}^h \cdot \mathbf{G} \mathbf{u}^h + C_I (\frac{\mu}{\rho})^2 \mathbf{G} : \mathbf{G} \right]^{-\frac{1}{2}}$$

$$\tau_C = \frac{1}{tr(\mathbf{G})\tau_M}$$

$$\tau_T = \left[\frac{4}{\Delta t^2} + \mathbf{u}^h \cdot \mathbf{G} \mathbf{u}^h + C_I (\frac{\kappa}{\rho c_p})^2 \mathbf{G} : \mathbf{G} \right]^{-\frac{1}{2}}$$

where Δt is the time-step size, C_I is a positive constant [43], $\mathbf{G}$ is the element metric tensor calculated by the mapping from the iso-parametric element to its physical counterpart, and $tr\,\mathbf{G}$ is the trace of $\mathbf{G}$. $\mathbf{G}$ is defined as $G_{ij} = \frac{\partial \xi_k}{\partial x_i} \frac{\partial \xi_k}{\partial x_j}$ (Einstein summation notation is used), where $\boldsymbol{\xi}$ are the parametric coordinates.

The above formulation is temporally integrated by a generalized-α scheme [44]. Newton method is used to linearize the nodal nonlinear equations. The resulting linear systems are solved by using a generalized minimal residual method (GMRES) [45] with block preconditioning [23]. It should be noted that this is not the first application of VMS or stabilized methods to thermal fluid flow simulations. Several successful previous applications without phase transition can be found in [46–49]. The code is parallelized by using Message Passing Interface (MPI). All the simulations presented next are executed in Frontera at Texas Advanced Computing Center.

3. Numerical examples

3.1. Laser spot weld pool flows

We first use the proposed formulation to simulate a laser welding process without material deposition. Fig. 3 (left) shows the problem setup. A bulk of metal based on steel (Fe–S system), with sulfur as the active element, is melted by a stationary heat laser applied on the top surface. The material properties are listed in Table 1. The heat

Table 1
Material properties.

Name	Notation (units)	Value
Gas density	ρ_a (kg m^{-3})	0.864
Gas heat capacity	$c_{p,a}$ (J kg^{-1} K^{-1})	680
Gas thermal conductivity	k_a (W m^{-1} K^{-1})	0.028
Metal density	ρ_l, ρ_s (kg m^{-3})	8100
Viscosity of liquid metal	μ_l (Pa s)	0.006
Liquid heat capacity	$c_{p,l}$ (J kg^{-1} K^{-1})	723.14
Liquid thermal conductivity	k_l (W m^{-1} K^{-1})	22.9
Solid heat capacity	$c_{p,s}$ (J kg^{-1} K^{-1})	627.0
Solid thermal conductivity	k_s (W m^{-1} K^{-1})	22.9
Liquidus temperature	T_l (K)	1630
Solidus temperature	T_s (K)	1610
Latent heat of fusion	L (J kg^{-1})	2.508×10^5
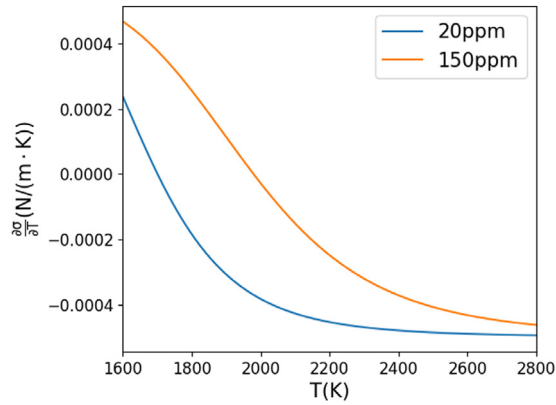
Fig. 2. Marangoni coefficient $\frac{\partial \sigma}{\partial T}$ as a function of temperature T for two sulfur activities ($a_i = 20$ ppm and $a_i = 150$ ppm).

laser q_{in} takes the following form

$$q_{in} = \begin{cases} \frac{\eta Q}{\pi r_b^2} & r \leq r_b \\ 0 & r > r_b \end{cases} \tag{23}$$

where $\eta = 0.13$ is the absorptivity, $Q = 5200$ W is the laser power, $r_b = 1.4$ mm is the laser radius. The melt pool shape and melt pool fluid dynamics largely depend on the Marangoni coefficient $\frac{\partial \sigma}{\partial T}$. According to the model in [50], $\frac{\partial \sigma}{\partial T}$ is a function of temperature and sulfur concentration, defined as

$$\frac{\partial \sigma}{\partial T} = \frac{d\sigma}{dT}|_0 - R\tau_s ln(1 + Ka_i) - \frac{Ka_i}{1 + Ka_i} \frac{\tau_s(\Delta H^0 - \Delta H^M)}{T} \tag{24}$$

where $\frac{d\sigma}{dT}|_0$ is the pure metal Marangoni coefficient, τ_s is the surface excess at saturation, R is the gas constant. $K = k_i exp(\frac{-\Delta H^0}{RT})$ is the equilibrium constant for segregation, where k_i is the entropy factor, ΔH^0 is the standard heat of absorption, ΔH^M is the partial molar enthalpy of species mixing in the solution. a_i is the sulfur weight percentage. The values of these parameters are summarized in Table 2. In this paper, two sulfur activities $a_i = 0.002\%$–wt (20 ppm) and $a_i = 0.015\%$–wt (150 ppm) are investigated. The corresponding $\frac{\partial \sigma}{\partial T}$ as a function of temperature is plotted in Fig. 2.

We simulate the problem with linear tetrahedral elements. As shown in Fig. 3 (right), the computational domain is a cylinder with a radius of 7 mm and a height of 20 mm. The metal occupies the bottom half of the domain. A refined cylinder with a radius of 3 mm and a height of 12 mm is placed in the domain center to better capture the temperature and fluid dynamics. The mesh size gradually grows from the refined region to the outer boundaries
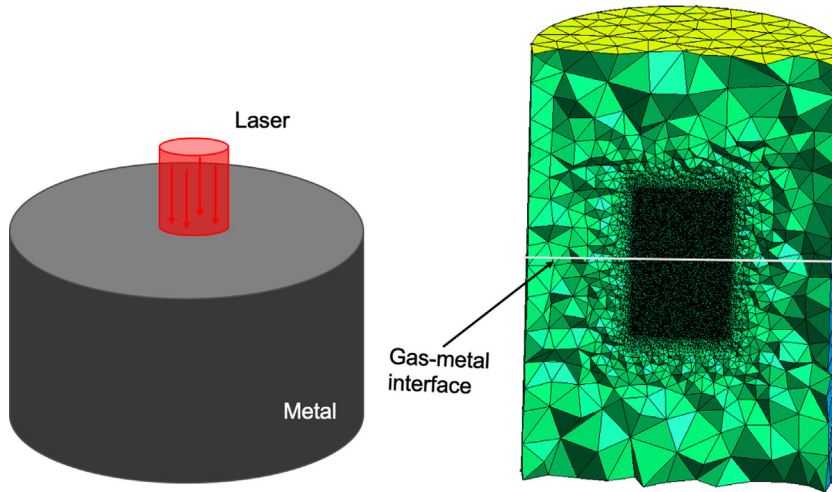
Fig. 3. Diagram of laser spot weld pool flow. Left: Problem setup. Right: Mesh.

Table 2
Parameters of Maragoni coefficient.

Name	Notation (units)	Value
Pure metal Marangoni coefficient	$\frac{d\sigma}{dT}\rvert_0$ (N m^{-1} K^{-1})	-5×10^{-4}
Saturation surface excess	τ_s (kmole m^{-2})	1.3×10^{-8}
Entropy factor	$k_i(-)$	3.18×10^{-3}
Standard heat of absorption	ΔH^0 (J kmole^{-1})	-1.66×10^8
Partial molar enthalpy of species	ΔH^M (J kmole^{-1})	0
Sulfur activity	a_i (%)	$0.002, 0.015$

from 0.08 mm to 2 mm. The total number of nodes and elements of the mesh are and 351,012 and 1,612,787, respectively.

Since no material is deposited, a flat air–metal interface is assumed. The Marangoni effect, no penetration boundary condition, and heat source are applied on the air–metal interface by using the CSF models specified in Eq. (18)- (20). No heat flux and no-slip boundary conditions are applied on the three surfaces of the cylindrical domain. The simulations were run with 192 processors with $\Delta t = 1 \times 10^{-3}$ s. This problem was investigated experimentally in [51] and computationally in [23] using a liquid–solid model. The results are used for comparison next.

Figs. 4 and 5 show the temperature contour, melt pool shape, and fluid velocity vectors scaled by their magnitude for the cases with two sulfur activities. The velocity vectors are tangential to the air–metal interface, which indicates that the no penetration boundary condition is enforced well by the CSF model. As shown in Fig. 2, the Marangoni coefficient has different signs in the melt pools for $a_i = 20$ ppm and $a_i = 150$ ppm cases, which leads to different melt pool shape and opposite flow circulations, as depicted in Fig. 4. In the $a_i = 20$ ppm case, the Marangoni coefficient is mainly positive in the melt pool. The higher surface force in higher temperature drives the flow from the boundary to the center and digs a narrow and deep melt pool (see Fig. 5 (left)). In contrast, the Marangoni coefficient in the $a_i = 150$ ppm case is mainly negative in the melt pool. The higher surface force in lower temperature drives the flow from the center to the boundary and results in a wide and shallow melt pool (see Fig. 5 (right)). Fig. 6 shows the time history of melt pool dimensions. Experimental measurements from [51] and numerical predictions from [23] are also plotted for comparison. Good agreements are obtained.

3.2. Direct energy deposition of SS-316L

A single-track direct energy deposition (DED) process is simulated to demonstrate the proposed approach's predictive capability. The problem is set up as follows. A laser with a Gaussian profile scans across a flat SS-316L
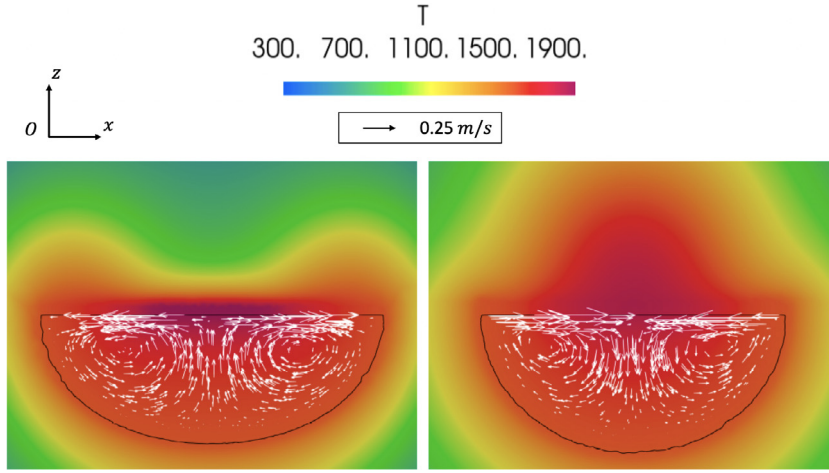
Fig. 4. Temperature (unit: K) and velocity (unit: m/s) vectors in melt pool (slice view). The black solid line indicates the melt pool boundary. Left: 20 ppm. Right: 150 ppm.
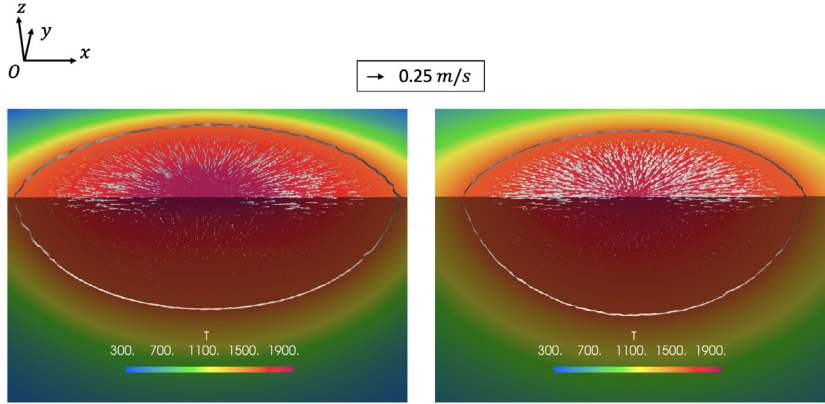
Fig. 5. Temperature (unit: K) and velocity (unit: m/s) vectors in melt pool (3D view). The black solid line indicates the melt pool boundary. Left: 20 ppm. Right: 150 ppm.

substrate with an initial temperature of $T_0 = 300$ K. During the scanning, the nozzle around the laser simultaneously release SS-316L powders into the laser beam and deposit them onto the substrate. When the particles reach the built surface, it is assumed that they have been heated up to the local temperature. Thus, the absorbed energy by the depositing material can be computed as

$$Q_v = \dot{m} \int_{T_0}^{T} c_p(\tau) d\tau \tag{25}$$

The remaining laser energy entering the metal through the CSF model is

$$Q_T = \frac{d(\eta_p Q - Q_v)}{\pi r_b^2} exp(-d \frac{\|\mathbf{x} - \mathbf{x_c}\|^2}{r_b^2})(\mathbf{n} \cdot \mathbf{e}_3)\delta_\epsilon \tag{26}$$

The properties of SS-316L and manufacturing parameters utilized in the paper are listed in Tables 3 and 4. The simulations make use of a box with dimensions of $30.0 \times 5.0 \times 4.2$ mm. Structured hexahedral elements are used. A refined region with element length 0.06 mm is designed along the track to better capture the temperature and fluid dynamics. The generated mesh consists of 496,571 nodes and 388,960 elements. The simulation is performed with $\Delta t = 0.25 \times 10^{-3}$ s until the melt pool reaches the quasi-steady state.
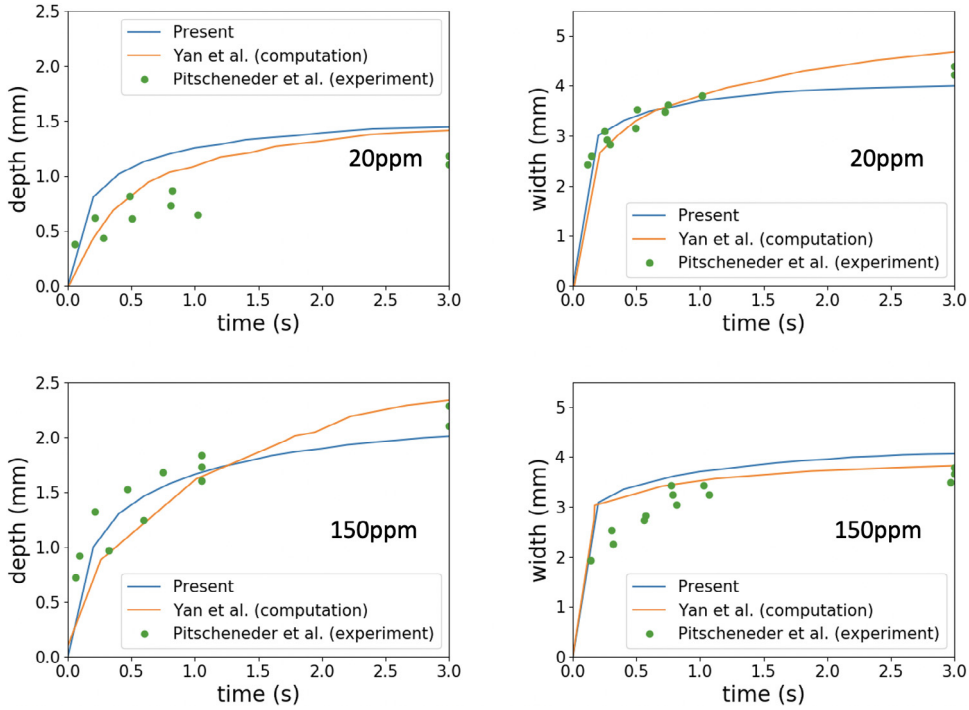
Fig. 6. Time history of melt pool dimensions. Experimental results from [51] and numerical predictions from [23] are also plotted for comparison.

Fig. 7 shows the temperature contour, melt pool shape, and velocity vectors in the gas and the melt pool at t = 0.25 s, 0.5 s, and 0.75 s. As the laser moves forward, the constant negative Marangoni coefficient (see Table 3) drives the flow from high temperature to low temperature, leading to a long flow circulation region behind. Fig. 8 shows the built cross-section behind the laser and velocity vectors in the melt pool. The experimental image is also included for comparison. The theoretical deposit geometry model gives a very similar deposit shape to the experimental measurement. Besides, the predictive melt pool agrees well with the dilution region measured by the experiment. Fig. 9 shows the time history of melt pool dimension development. It takes a longer time for the length than width/depth to become stable. When the melt pool reaches the quasi-steady state (the shape does not change), the dimensions are measured and listed in Table 5.

Cooling rate is a vital variable in metal AM, which has an unmatched effect on micro-structure evolution [20,52], such as dendrite growth. Previous research indicated that the mechanical strength of additive manufactured parts is closely related to cooling rate. Fig. 10 shows the temperature profile at the quasi-steady state along the centerline of the deposit. In this paper, cooling rate is calculated at the centerline of the deposit by $K_v = \frac{T_l - T_s}{t_v}$, where t_v is the time of the cooling process takes from liquidus temperature to solidus temperature. We employ the theoretical model from [53] to evaluate the effect of cooling rate on mechanical properties. Firstly, the average magnitude of secondary dendrite arm spacing (SDAS), λ, is computed as

$$\lambda = 50(K_v)^{-0.4} \tag{27}$$

The unit of λ is μm. Moreover, the average hardness H_v related to yield strength of SS-316L takes the following form [21]

$$H_v = 3\sigma_y(0.1)^{-\frac{1}{4}} \tag{28}$$

where σ_y is the yield strength, which is a also function of average magnitude of SDAS, defined as

$$\sigma_y = \sigma_0 + \frac{K_y}{\sqrt{\lambda}} \tag{29}$$

Table 3

Material properties of SS-316L.

Name	Notation (units)	Value
Gas density	ρ_g (kg m^{-3})	0.864
Liquid density	ρ_l (kg m^{-3})	7800
Solid density	ρ_s (kg m^{-3})	7800
Gas heat capacity	$c_{p,g}$ (J kg^{-1} K^{-1})	680
Liquid heat capacity	$c_{p,l}$ (J kg^{-1} K^{-1})	769.9
Solid heat capacity	$c_{p,s}$ (J kg^{-1} K^{-1})	$330.9 + 0.563T - 4.015 \times 10^{-4}T^2$ $+9.465 \times 10^{-8}T^3$
Gas conductivity	k_g (W m^{-1} K^{-1})	0.028
Liquid conductivity	k_l (W m^{-1} K^{-1})	40.95
Solid conductivity	k_s (W m^{-1} K^{-1})	11.82+0.0106T
Liquidus temperature	T_l (K)	1733
Solidus temperature	T_s (K)	1693
Latent heat of fusion	L (kJ kg^{-1} K)	272
Dynamics viscosity	μ (Pa s)	0.007
Surface tension	σ (N m^{-1})	1.5
Marangoni coefficient	$\frac{\partial \sigma}{\partial T}$ (N m^{-1} K^{-1})	-4×10^{-4}
Ambient temperature	T_∞ (K)	300

Table 4

DED parameters.

Name	Notation (units)	Value
Laser power	Q (W)	2500
Laser moving speed	V_s (m s^{-1})	0.0106
Laser radius	r_b (m)	0.002
distribution factor	d (−)	2.0
Powder flow rate	$\dot{m}$ (kg s^{-1})	0.25×10^{-3}

Table 5

Quasi-steady melt pool dimensions.

| Length (mm)	Width (mm)	Depth (mm)
6.80	3.40	1.35

Table 6

Cooling rate K_v, average magnitude of SDAS λ, and average hardness H_v.

|	Cooling rate (K s^{-1})	SDAS (μm)	Hardness (MPa)
Present	937	3.24	2107.5
Simulation [20]	608	3.85	2039.0
Experiment [20]	–	3.27 ± 0.65	2014.5 ± 44.5

where σ_0 and K_y are material-dependent coefficients, whose values are 240 MPa and 279 MPa μm$^{\frac{1}{2}}$ for SS-316L, respectively [54]. Based these models, we list the predicted cooling K_v, average magnitude of SDAS λ, and averaged hardness H_v in Table 6, which shows good agreement with the experimental and simulation data obtained from [20].

4. Conclusion

In this paper, we propose an effective thermal multi-phase flow framework for metal additive manufacturing (AM), particularly directed energy deposition (DED) processes. In contrast to the presumed deposit shapes used in the literature, a new deposit geometry model is developed based on an energy minimization function with a mass conservation constraint. A moving distance function with respect to the deposit geometry is then constructed to distinguish the air and metal phases. This interface-capture approach gives the freedom to deploy the thermal fluid
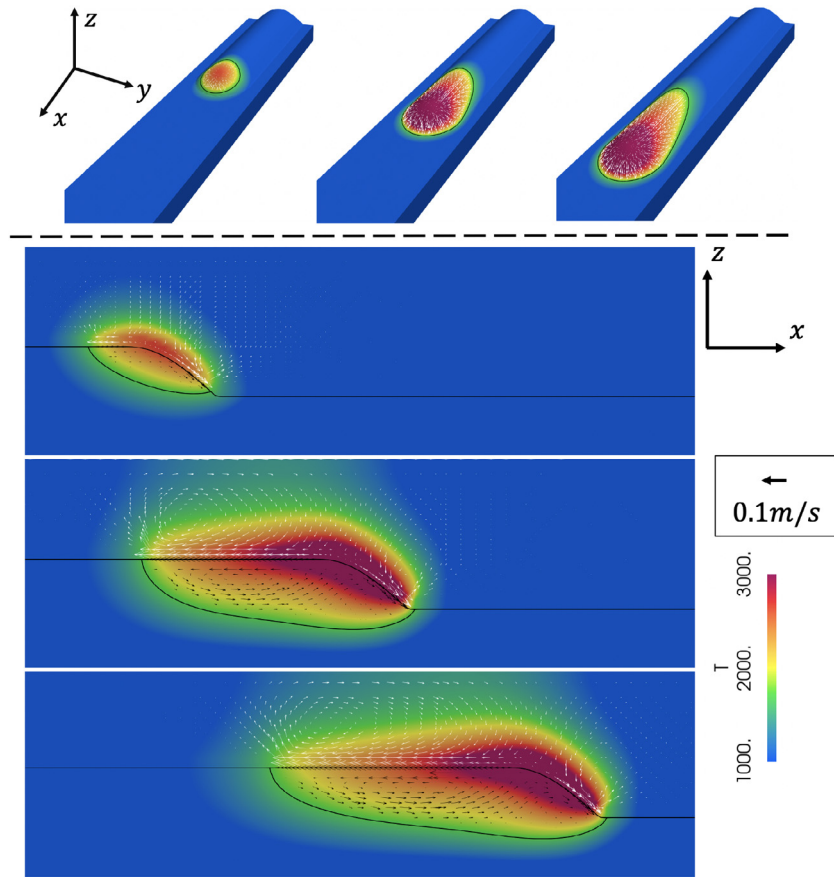
Fig. 7. Velocity vectors (unit: m/s) and temperature (unit: K) contour at $t = 0.25$ s, 0.5 s, and 0.75 s (from left to right and from top to bottom). The solid line indicates the melt pool boundary and gas–metal interface. The velocity vectors are plotted in white for the gas phase and in black for the metal phase.
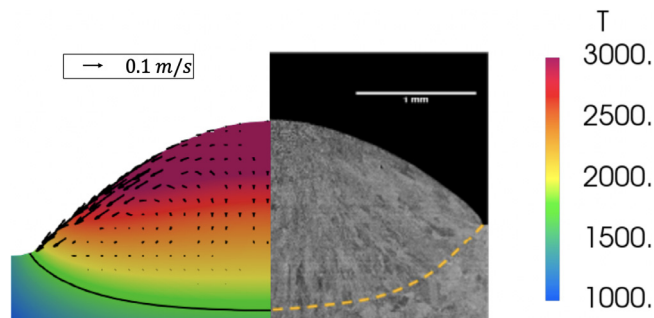

Fig. 8. Cross-section of the deposit: Temperature contour (unit: K) and velocity vectors (unit: m/s) in the melt pool. Left: Present prediction (the solid line indicates the boundary of the melt pool). Right: Experimental image from [20] (the dotted yellow lines indicates the edge of the dilution region).

model to any mesh type without explicitly needing to activate the solid elements in a mesh. We validate the proposed method on two representative metal manufacturing problems. Good agreement with experimental measurements is achieved. For the DED processes of SS-316L, the model can accurately predict the melt pool dimensions, fluid dynamics, and the average magnitude of SDAS and hardness.
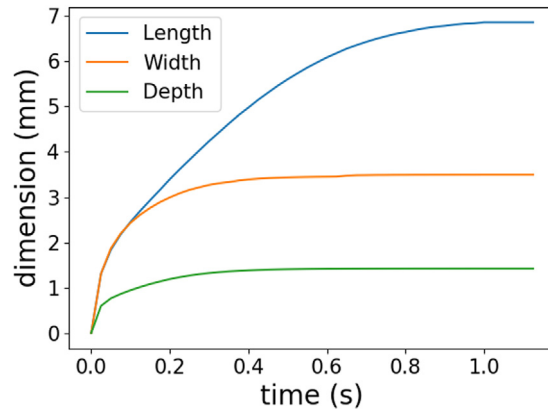
Fig. 9. Time history of melt pool dimensions.
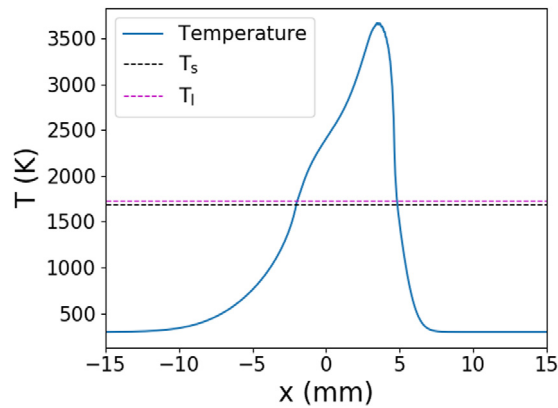
Fig. 10. Temperature profile along the centerline of the deposit at the quasi-steady state.

Some parts of the proposed formulation can be improved. Firstly, due to the complex fluid motion in the melt pool, the energy function in the minimization problem does not consider the kinetic energy, which may or may not affect the deposit geometry. Secondly, a large portion of the mesh is pre-refined along the track to capture the physics. Efficiency can be improved by incorporating adaptive mesh refinement (AMR) methods into the formulation. AMR is especially attractive for modeling multi-track and multi-layer metal AM processes. These issues will be addressed in future work.

Declaration of competing interest

The authors declare that they have no known competing financial interests or personal relationships that could have appeared to influence the work reported in this paper.

Acknowledgments

References

[1] W. Frazier, Metal additive manufacturing: a review, J. Mater. Eng. Perform. 23 (6) (2014) 1917–1928.

[2] C. Noble, A. Anderson, N. Barton, J. Bramwell, A. Capps, M. Chang, J. Chou, D. Dawson, E. Diana, T. Dunn, Ale3d: An Arbitrary Lagrangian-Eulerian Multi-Physics Code, Technical report, Lawrence Livermore National Lab.(LLNL), Livermore, CA (United States), 2017.

[3] S. Khairallah, A. Anderson, A. Rubenchik, W. King, Laser powder-bed fusion additive manufacturing: Physics of complex melt flow and formation mechanisms of pores, spatter, and denudation zones, Acta Mater. 108 (2016) 36–45.

[4] T.T. Roehling, S. Wu, S.A. Khairallah, J.D. Roehling, S.S. Soezeri, M.F. Crumb, M.J. Matthews, Modulating laser intensity profile ellipticity for microstructural control during metal additive manufacturing, Acta Mater. 128 (2017) 197–206.

[5] S. Khairallah, A. Martin, J. Lee, G. Guss, N. Calta, J. Hammons, M. Nielsen, K. Chaput, E. Schwalbach, M. Shah, G. Chapman, T. Willey, A. Rubenchik, A. Anderson, Y. Wang, M. Matthews, W. King, Controlling interdependent meso-nanosecond dynamics and defect generation in metal 3d printing, Science 368 (6491) (2020) 660–665.

[6] S. Lin, Numerical Methods and High Performance Computing for Modeling Metallic Additive Manufacturing Processes at Multiple Scales (Ph.D. thesis), Northwestern University, 2019.

[7] S. Lin, Z. Gan, J. Yan, G. Wagner, A conservative level set method on unstructured meshes for modeling multiphase thermo-fluid flow in additive manufacturing processes, Comput. Methods Appl. Mech. Engrg. 372 (2020) 113348.

[8] W. Yan, W. Ge, Y. Qian, S. Lin, B. Zhou, W.K. Liu, F. Lin, G.J. Wagner, Multi-physics modeling of single/multiple-track defect mechanisms in electron beam selective melting, Acta Mater. 134 (2017) 324–333.

[9] W. Yan, Y. Qian, W. Ge, S. Lin, W.K. Liu, F. Lin, G.J. Wagner, Meso-scale modeling of multiple-layer fabrication process in selective electron beam melting: inter-layer/track voids formation, Mater. Des. 141 (2018) 210–219a.

[10] W. Yan, S. Lin, O. Kafka, Y. Lian, C. Yu, Z. Liu, J. Yan, S. Wolff, H. Wu, E. Ndip-Agbor, M. Mozaffar, K. Ehmann, J. Cao, G. Wagner, W. Liu, Data-driven multi-scale multi-physics models to derive process–structure–property relationships for additive manufacturing, Comput. Mech. 61 (5) (2018) 521–541b.

[11] W. Yan, W. Ge, J. Smith, S. Lin, O. Kafka, F. Lin, W. Liu, Multi-scale modeling of electron beam melting of functionally graded materials, Acta Mater. 115 (2016) 403–412.

[12] H. Chen, W. Yan, Spattering and denudation in laser powder bed fusion process: multiphase flow modelling, Acta Mater. (2020).

[13] C. Panwisawas, C. Qiu, M.J. Anderson, Y. Sovani, R.P. Turner, M.M. Attallah, J.W. Brooks, H.C. Basoalto, Mesoscale modelling of selective laser melting: Thermal fluid dynamics and microstructural evolution, Comput. Mater. Sci. 126 (2017) 479–490.

[14] X. Li, C. Zhao, T. Sun, W. Tan, Revealing transient powder-gas interaction in laser powder bed fusion process through multi-physics modeling and high-speed synchrotron x-ray imaging, Addit. Manuf. (2020) 101362.

[15] S. Wang, L. Zhu, J. Fuh, H. Zhang, W. Yan, Multi-physics modeling and gaussian process regression analysis of cladding track geometry for direct energy deposition, Opt. Lasers Eng. (ISSN: 0143-8166) 127 (2020) 105950.

[16] Y. Cao, S. Zhu, X. Liang, W. Wang, Overlapping model of beads and curve fitting of bead section for rapid manufacturing by robotic mag welding process, Robot. Comput.-Integr. Manuf. 27 (2011) 641–645.

[17] D. Corbin, A. Nassar, E. Reutzel, A. Beese, N. Kistler, Effect of directed energy deposition processing parameters on laser deposited inconel® 718: External morphology, J. Laser Appl. 29 (2) (2017) 022001.

[18] J. Xiong, G. Zhang, J. Hu, L. Wu, Bead geometry prediction for robotic gmaw-based rapid manufacturing through a neural network and a second-order regression analysis, J. Intell. Manuf. 25 (2014).

[19] C. Doumanidis, Y. Kwak, Multivariable adaptive control of the bead profile geometry in gas metal arc welding with thermal scanning, Int. J. Press. Vessels Pip. 79 (4) (2002) 251–262.

[20] G.L. Knapp, T. Mukherjee, J.S. Zuback, H.L. Wei, T.A. Palmer, A. De, T. Debroy, Building blocks for a digital twin of additive manufacutring, Acta Mater. (2017).

[21] V. Manvatkar, A. De, T. Debroy, Heat transfer and material flow during laser assisted multi-layer additive manufacturing, J. Appl. Phys. (2014).

[22] J. Brackbill, D. Kothe, C. Zemach, A continuum method for modeling surface tension, J. Comput. Phys. 100 (2) (1992) 335–354.

[23] J. Yan, W. Yan, S. Lin, G.J. Wagner, A fully coupled finite element formulation for liquid–solid–gas thermo-fluid flow with melting and solidification, Comput. Methods Appl. Mech. Engrg. 336 (2018) 444–470c.

[24] J. Yan, S. Lin, Y. Bazilevs, G.J. Wagner, Isogeometric analysis of multi-phase flows with surface tension and with application to dynamics of rising bubbles, Comput. & Fluids 179 (2019) 777–789.

[25] S. Lin, J. Yan, D. Kats, G. Wagner, A volume-conserving balanced-force level set method on unstructured meshes using a control volume finite element formulation, J. Comput. Phys. 380 (2019) 119–142.

[26] T.J.R. Hughes, A. Oberai, L. Mazzei, Large eddy simulation of turbulent channel flows by the variational multiscale method, Phys. Fluids 13 (6) (2001) 1784–1799a.

[27] T.J.R. Hughes, L. Mazzei, A. Oberai, A. Wray, The multiscale formulation of large eddy simulation: Decay of homogeneous isotropic turbulence, Phys. Fluids 13 (2) (2001) 505–512b.

[28] Y. Bazilevs, V. Calo, T.J.R. Hughes, Y. Zhang, Isogeometric fluid–structure interaction: theory, algorithms, and computations, Comput. Mech. 43 (1) (2008) 3–37.

[29] R. Khurram, A. Masud, A multiscale/stabilized formulation of the incompressible navier–stokes equations for moving boundary flows and fluid–structure interaction, Comput. Mech. 38 (4–5) (2006) 403–416.

[30] Y. Otoguro, H. Mochizuki, K. Takizawa, T. Tezduyar, Space–time variational multiscale isogeometric analysis of a tsunami-shelter vertical-axis wind turbine, Comput. Mech. (2020) 1–18.

[31] J. Liu, A. Marsden, A unified continuum and variational multiscale formulation for fluids, solids, and fluid–structure interaction, Comput. Methods Appl. Mech. Engrg. 337 (2018) 549–597.

[32] T. Hughes, G. Feijóo, L. Mazzei, J. Quincy, The variational multiscale method—a paradigm for computational mechanics, Comput. Methods Appl. Mech. Engrg. 166 (1–2) (1998) 3–24.

[33] Y. Bazilevs, V.M. Calo, J.A. Cottrel, T.J.R. Hughes, A. Reali, G. Scovazzi, Variational multiscale residual-based turbulence modeling for large eddy simulation of incompressible flows, Comput. Methods Appl. Mech. Engrg. 197 (2007) 173–201.

[34] A.N. Brooks, T.J.R. Hughes, Streamline upwind/Petrov-Galerkin formulations for convection dominated flows with particular emphasis on the incompressible Navier–Stokes equations, Comput. Methods Appl. Mech. Engrg. 32 (1982) 199–259.

[35] T.E. Tezduyar, Stabilized finite element formulations for incompressible flow computations, Adv. Appl. Mech. 28 (1992) 1–44.

[36] T.E. Tezduyar, Y. Osawa, Finite element stabilization parameters computed from element matrices and vectors, Comput. Methods Appl. Mech. Engrg. 190 (2000) 411–430.

[37] T.J.R. Hughes, G. Scovazzi, L.P. Franca, Multiscale and stabilized methods, in: Encyclopedia of Computational Mechanics, John Wiley & Sons, 2004.

[38] M.C. Hsu, Y. Bazilevs, V.M. Calo, T.E. Tezduyar, T.J.R. Hughes, Improving stability of stabilized and multiscale formulations in flow simulations at small time steps, Comput. Methods Appl. Mech. Engrg. 199 (2010) 828–840.

[39] A. Masud, R. Calderer, A variational multiscale stabilized formulation for the incompressible navier–stokes equations, Comput. Mech. 44 (2) (2009) 145–160.

[40] L. Zhu, S. Goraya, A. Masud, Interface-capturing method for free-surface plunging and breaking waves, J. Eng. Mech. 145 (11) (2019) 04019088.

[41] R. Calderer, L. Zhu, R. Gibson, A. Masud, Residual-based turbulence models and arbitrary lagrangian–eulerian framework for free surface flows, Math. Models Methods Appl. Sci. 25 (12) (2015) 2287–2317.

[42] A. Masud, R. Calderer, Residual-based turbulence models for moving boundary flows: hierarchical application of variational multiscale method and three-level scale separation, Internat. J. Numer. Methods Fluids 73 (3) (2013) 284–305.

[43] C. Johnson, Numerical Solution of Partial Differential Equations by the Finite Element Method, Cambridge University Press, Sweden, 1987.

[44] J. Chung, G.M. Hulbert, A time integration algorithm for structural dynamics with improved numerical dissipation: the generalized-α method, J. Appl. Mech. 60 (2) (1993) 371–375.

[45] Y. Saad, M. Schultz, GMRES: A generalized minimal residual algorithm for solving nonsymmetric linear systems, SIAM J. Sci. Stat. Comput. 7 (1986) 856–869.

[46] R. Codina, J. Principe, Dynamic subscales in the finite element approximation of thermally coupled incompressible flows, Internat. J. Numer. Methods Fluids 54 (6–8) (2007) 707–730.

[47] R. Codina, N. Hernández, Approximation of the thermally coupled mhd problem using a stabilized finite element method, J. Comput. Phys. 230 (4) (2011) 1281–1303.

[48] B. Schrefler, R. Codina, F. Pesavento, J. Principe, Thermal coupling of fluid flow and structural response of a tunnel induced by fire, Internat. J. Numer. Methods Engrg. 87 (1–5) (2011) 361–385.

[49] T. Tezduyar, S. Ramakrishnan, S. Sathe, Stabilized formulations for incompressible flows with thermal coupling, Internat. J. Numer. Methods Fluids 57 (9) (2008) 1189–1209.

[50] P. Sahoo, T. Debroy, M. Mcnallan, Surface tension of binary metal—surface active solute systems under conditions relevant to welding metallurgy, Metall. Trans. B 19 (1988) 483–491.

[51] W. Pitscheneder, Tarasankar Debroy, K. Mundra, R. Ebner, Role of sulfur and processing variables on the temporal evolution of weld pool geometry during multikilowatt laser beam welding of steels, Weld. J. 75 (1996) 71s–80s.

[52] Z. Gan, Y. Lian, S.E. Lin, K.K. Jones, W.K. Liu, G.J. Wagner, Benchmark study of thermal behavior, surface topography, and dendritic microstructure in selective laser melting of inconel 625, Integr. Mater. Manuf. Innov. (2019).

[53] H. Yin, S. Felicelli, Dendrite growth simulation during solidification in the lens process, Acta Mater. 58 (2010) 1455–1465.

[54] B.P. Kashyap, K. Tangri, On the hall-petch relationship and substructural evolution in type 316l stainless steel, Acta Mater. 58 (1995) 1455–1465.